

# Searching for star-planet interactions in GJ 486 at radio wavelengths with the uGMRT

L. Peña-Moñino<sup>1</sup>, M. Pérez-Torres<sup>1,2</sup>, D. Kansabanik<sup>3</sup>, G. Blázquez-Calero<sup>1</sup>, R. D. Kavanagh<sup>4,5</sup>, J. F. Gómez<sup>1</sup>, J. Moldón<sup>1</sup>, A. Alberdi<sup>1</sup>, P. J. Amado<sup>1</sup>, G. Anglada<sup>1</sup>, J. A. Caballero<sup>9</sup>, A. Mohan<sup>7</sup>, P. Leto<sup>8</sup>, M. Narang<sup>6</sup>, M. Osorio<sup>1</sup>, D. Revilla<sup>1</sup>, and C. Triguero<sup>8</sup>

<sup>1</sup> IAA-CSIC, Instituto de Astrofísica de Andalucía, Glorieta de la Astronomía s/n, 18008, Granada, Spain  
e-mail: [lpm@iaa.es](mailto:lpm@iaa.es)

<sup>2</sup> School of Sciences, European University Cyprus, Diogenes street, Engomi, 1516 Nicosia, Cyprus

<sup>3</sup> Cooperative Programs for the Advancement of Earth System Science, University Corporation for Atmospheric Research, Boulder, CO, USA

<sup>4</sup> ASTRON, Netherlands Institute for Radio Astronomy, Oude Hoogeveensedijk 4, Dwingeloo, 7991 PD, The Netherlands

<sup>5</sup> Anton Pannekoek Institute for Astronomy, University of Amsterdam, 1090 GE Amsterdam, the Netherlands

<sup>6</sup> Academia Sinica Institute of Astronomy & Astrophysics, Taipei 10617, Taiwan

<sup>7</sup> Goddard Space Flight Center, Greenbelt, Maryland, USA

<sup>8</sup> INAF-Osservatorio Astrofisico di Catania, Via Santa Sofia 78, 95123 Catania, Italy

<sup>9</sup> Centro de Astrobiología (CSIC-INTA), Campus ESAC, Camino Bajo del Castillo s/n, 28692 Villanueva de la Cañada, Madrid, Spain

Received 8 August 2024; accepted 21 November 2024

## ABSTRACT

**Aims.** We search for radio emission from star-planet interactions in the M-dwarf system GJ 486, which hosts an Earth-like planet.

**Methods.** We observed the GJ 486 system with the upgraded Giant Metrewave Radio Telescope (uGMRT) from 550 to 750 MHz in nine different epochs, between October 2021 and February 2022, covering almost all orbital phases of GJ 486b from different orbital cycles. We obtained radio images and dynamic spectra of the total and circularly polarized intensity for each individual epoch.

**Results.** We do not detect any quiescent radio emission in any epoch above  $3\sigma$ . Similarly, we do not detect any bursty emission in our dynamic spectra. While we cannot completely rule out that the absence of a radio detection is due to time variability of the radio emission, or to the maximum electron-cyclotron maser emission being below our observing range, this seems unlikely. We discuss two possible scenarios: an intrinsic dim radio signal, or alternatively, that the anisotropic beamed emission pointed away from the observer. If the non-detection of radio emission from star-planet interaction in GJ 486 is due to an intrinsically dim signal, this implies that, independently of whether the planet is magnetized or not, the mass-loss rate is small ( $\dot{M}_* \lesssim 0.3 \dot{M}_\odot$ ) and that, concomitantly, the efficiency of the conversion of Poynting flux into radio emission must be low ( $\beta \lesssim 10^{-3}$ ). Free-free absorption effects are negligible, given the high value of the coronal temperature. Finally, if the anisotropic beaming pointed away from us, this would imply that GJ 486 has very low values of its magnetic obliquity and inclination.

**Key words.** instrumentation: interferometers – planet-star interactions – stars: flare, magnetic field

## 1. Introduction

M dwarfs, also known as “red dwarfs”, are the most common stars in the solar neighbourhood (e.g., [Reylé et al. 2021](#)). They are expected to preferentially host close-in rocky planets ([Sabotta et al. 2021](#); [Ribas et al. 2023](#)). The discovery of Proxima b, an Earth-sized, rocky planet within the habitability zone of its star Proxima Centauri ([Anglada-Escudé et al. 2016](#)), boosted the interest of the astronomical community, and the study of exoplanets and their potential habitability has blossomed in the last decade, thanks to space-based missions (e.g., Kepler, TESS), as well as to the exploitation of data taken with ground-based telescopes.

The discovery of the majority of exoplanets around M dwarfs, including rocky ones, has been done using radial velocity and transit measurements, while their discovery in the radio has been elusive despite decades of relentless efforts. The detection of auroral radio emission from an exoplanet would con-

firm the existence of such an exoplanet, and would inform us of its intrinsic magnetic field. The latter is a piece of information that cannot be provided by other means, which makes radio observations unique. Unfortunately, Earth and super-Earth exoplanets with plausible magnetic field strengths of up to a few Gauss would result in auroral radio emission from such an exoplanet at frequencies below the Earth’s ionospheric cutoff of  $\sim 10$  MHz, therefore making this radio emission undetectable from Earth. However, if an exoplanet is close enough to its host star that it is in the sub-Alfvénic regime, i.e., when the plasma speed relative to the exoplanet,  $v$ , is smaller than the Alfvén speed at the planet position,  $v_A$ , then energy and momentum can be transported upstream back to the star by Alfvén waves. Jupiter’s interaction with its Galilean satellites is a well-known example of sub-Alfvénic interaction, which results in copious auroral radio emission ([Zarka 2007](#)). The mechanism responsible for this emission is the electron-cyclotron maser (ECM) insta-

bility, which is a coherent mechanism yielding strong, variable, highly-polarized emission. The typical energies of the electrons involved in auroral radio emission are around 1 keV (Wu & Lee 1979), and for the case of the Io-Jupiter decameter emission, the range of energies can go up to about 20 keV (e.g. Lamy et al. 2022). In the case of magnetic star-planet interaction (SPI), the radio emission arises from the upper layers of the atmosphere of the host star, induced by the exoplanet moving through the stellar magnetosphere, and thus the relevant magnetic field is that of the star,  $B_*$ , not the exoplanet magnetic field. This makes a huge difference in the frequency where to search for this radio emission.

M dwarfs are excellent candidates to detect star-planet interaction at radio wavelengths, since they have surface magnetic fields of a few hundred Gauss, or even kGauss (Shulyak et al. 2019; Kochukhov 2021; Reiners et al. 2022), so the fundamental frequency of the cyclotron emission falls into the detection capabilities of existing radio interferometers. Sub-Alfvénic interaction is expected to yield detectable periodic radio emission via the ECM mechanism, as long as the Alfvén wave connects back to the star (e.g. Zarka 2007; Saur et al. 2013; Turnpenney et al. 2018; Vedantham et al. 2020; Pérez-Torres et al. 2021). The confirmation of this radio emission would provide a completely new method of exoplanet detection. Namely, one would expect to detect strong, highly circularly polarized radio emission at an observing frequency close to, or below, the maximum cyclotron frequency, and showing a periodic signal that correlates with the orbital period of the planet,  $P_{\text{orb}}$ , or the synodic period,  $P_{\text{syn}}^{-1} = P_{\text{rot}}^{-1} - P_{\text{orb}}^{-1}$ , where  $P_{\text{rot}}$  is the rotation period of the host star, although we note that the geometry of the system can result in a more complex relation.

In recent years, there have been several claims of exoplanet induced radio emission (GJ 1151b - Vedantham et al. 2020; Proxima b - Pérez-Torres et al. 2021; YZ Cet b - Pineda & Villadsen 2023; Triglio et al. 2023), but a solid confirmation is still lacking for those cases. For example, Narang et al. (2024) recently reported non-detections of GJ 1151 with the uGMRT at 150, 218, and 400 MHz. In this paper, we present the results from the longest monitoring radio campaign on the star-exoplanet M dwarf system GJ 486 - GJ 486b, using the upgraded Giant Metrewave Radio Telescope, uGMRT (Gupta et al. 2017). Our overall aim is to characterize the radio emission from this system, with the main goal of detecting radio emission due to magnetic SPI. We describe the GJ 486 – GJ 486b system in Section 2, and our observations and data analysis in Section 3. We present our results in Section 4 and discuss them in Section 5.

## 2. The GJ 486 – GJ 486b system

GJ 486 is a cool, nearby M3.5V star (Caballero et al. 2022; see also Table 1). It rotates at a rate roughly half of the Sun and, given its mass, it is very likely an almost fully convective star. Trifonov et al. (2021) reported the existence of an exoplanet, GJ 486b, using radial velocity (RV) measurements from the CARMENES survey (Quirrenbach et al. 2016) and TESS photometry (Ricker et al. 2014). GJ 486b has a radius and a mass slightly larger than the Earth, straddling the boundary between Earth-like planets and super-Earths. However, its bulk density ( $\rho \approx 7.0 \text{ g cm}^{-3}$ ) favors a massive terrestrial planet rather than an ocean one (Trifonov et al. 2021). Given the proximity of the GJ 486 system (8.1 pc from Earth), and the small separation of the planet to its host star ( $\lesssim 0.02$  au), GJ 486 showed promise for detecting radio emission arising from star-planet interaction.

Table 1: Parameters of the GJ 486 – GJ 486b system

Parameter	Value
<b>Star (GJ 486)</b>	
$\alpha$ (J2000)	12:47:56.62
$\delta$ (J2000)	+09:45:05.0
$\mu_\alpha \cos \delta$ [mas yr $^{-1}$ ]	-1008.267 $\pm$ 0.040
$\mu_\delta$ [mas yr $^{-1}$ ]	-460.034 $\pm$ 0.033
Spectral Type	M3.5V
$T_{\text{eff}}$ (K)	3291 $\pm$ 75
$M_*/M_\odot$	0.333 $\pm$ 0.019
$R_*/R_\odot$	0.339 $\pm$ 0.015
Distance [pc]	8.0827 $\pm$ 0.0021
$P_{\text{rot}}$ [days]	49.9 $\pm$ 5.5
<b>Planet (GJ 486b)</b>	
$P_{\text{orb}}$ [days]	1.4671205 $^{+0.0000012}_{-0.0000011}$
$a$ [au]	0.01713 $^{+0.00091}_{-0.00098}$
$i$ [degrees]	88.90 $^{+0.69}_{-0.84}$
$M_p/M_\oplus$	3.00 $^{+0.13}_{-0.13}$
$R_p/R_\oplus$	1.343 $^{+0.063}_{-0.062}$

All values from Caballero et al. (2022).

### 2.1. ECM frequency and magnetic field of GJ 486

If radio emission is produced on a planet via the ECM instability, then the intrinsic planetary magnetic field can be directly measured. The maximum cyclotron frequency is given by

$$\nu_c [\text{MHz}] = s \times 2.8 B, \quad (1)$$

where  $B$  is the local magnetic field, in Gauss, and  $s$  is the harmonic number of the cyclotron frequency. ECM emission is observed essentially from the fundamental ( $s = 1$ ) (Melrose & Dulk 1982). However, the detection of radio emission from star-planet interaction could be feasible if the planet is in the sub-Alfvénic regime, as mentioned in Sect. 1. In this case, the relevant local magnetic field in Eq. 1 is that of the star,  $B_*$ . Using high-resolution spectral measurements with CFHT/ESPaDOnS, Moutou et al. (2017) determined a total surface magnetic field value of  $B_* f = 1.6 \pm 0.3$  kG for GJ 486, where  $f$  is the filling factor (the fraction of the stellar surface covered with magnetic field). Two filling factors could be considered here, namely the Stokes I and V filling factors,  $f_I$  and  $f_V$  respectively (Morin et al. 2008). However, the relevant one is  $f_V$ , which refers to the fraction of the field that manifests as a large-scale surface magnetic field, as opposed to  $f_I$ , which also takes into account smaller-scale field that may cancel out at larger scales, and is much more poorly constrained. From spectropolarimetric observations of a sample of mid M-dwarf stars of spectral types from M3 to M4.5, Morin et al. (2008) found that  $f_V$  is in the range from 0.10 to 0.15, with typical uncertainties of 0.03 in those values. Here, we used  $f = 0.15$ , which results in an average stellar magnetic field value of  $B_* = 240 \pm 45$  G. With this value of  $B_*$ , the maximum cyclotron frequency would then be  $\nu_c = 2.8 B_* = 672 \pm 126$  MHz, and  $\nu_c = 1344 \pm 252$  MHz for  $s = 1$  (fundamental ECM emission) and  $s = 2$  (second harmonic), respectively. We note that, since  $B_* = 240 \pm 45$  G is the average value of the magnetic field in the surface of the star, the value near the (magnetic) poles of the star, where the ECM is most likely produced, has a larger value. On the other hand, ECM emission can be generated at

some height above the stellar surface, where the local magnetic field would be smaller. We therefore assumed a nominal value of  $B_* = 240$  G, and carried out observations with the uGMRT in band 4 (550 – 900 MHz), which covers the relevant frequency range to search for ECM radio emission that could arise from star-planet interaction in the GJ 486 system.

## 2.2. X-rays from GJ 486

Stellar X-ray and radio (quiescent) activity correlate well (Güdel et al. 1993). Hence, host stars that are strong X-ray emitters would be expected to be also strong radio emitters, which could jeopardize the search for radio emission from star-planet interaction.

GJ 486 was not detected in X-rays with ROSAT (upper limit of  $f_x = 5.37 \times 10^{-14}$  erg s<sup>-1</sup>cm<sup>-2</sup>; Stelzer et al. 2013). However, recent XMM-Newton observations by Sanz-Forcada et al. (2024) resulted in a clear detection of GJ 486 in X-rays, with a flux at Earth of  $f_x = 4.05 \times 10^{-15}$  erg s<sup>-1</sup>cm<sup>-2</sup>. Using the relationship between radio and X-ray luminosities for M dwarf stars from Güdel et al. (1993), the X-ray luminosity of GJ 486 would result in a corresponding radio flux density of the star of a few  $\mu$ Jy. Therefore, the expected quiescent radio emission from the star should be negligible.

## 3. Observations and data processing

We observed GJ 486 with uGMRT on 30 October, 7, 9, 14, 16, 19 and 20 November 2021, and 14 January and 22 February 2022. We show in Fig. 1 the orbital phase coverage of our observations, which span almost the entire orbital phase of GJ 486b, and spread out over more than two full rotation periods of the star.

We observed GJ 486 at a central frequency of 650 MHz, using a bandwidth of 200 MHz and a standard integration time of 10.7 s. We used 2048 channels in total, for a channel width of 97.7 kHz. Given the high proper motion of GJ 486 (Table 1), we centered all our observations at  $\alpha(J2000.0) = 12^{\text{h}} 47^{\text{m}} 56.00^{\text{s}}$  and  $\delta(J2000.0) = 09^{\circ} 45' 05.00''$ . Each observing epoch lasted typically three to four hours, and we used a duty cycle of about 35 minutes, with 30 minutes on our target and 5 minutes on the quasar 3C 286, which we used as bandpass, flux and phase calibrator. The angular distance between this calibrator and GJ 486 is of  $\approx 23^{\circ}$ .

We performed all calibration steps using the Common Astronomy Software Application (CASA; McMullin et al. 2007; The CASA Team 2022), version casa-6.2.1-7-pipeline-2021.2.0.128. First, we used task `flagdata` to flag edge frequency channels of the observing band as well as frequency channels affected by strong radio frequency interference (RFI). Followed by this, we flagged dead antennas as well as 10 seconds at the start and end of each scan. We did this initial flagging on both 3C 286 and our target field, GJ 486. Afterwards, we performed an initial delay, bandpass and gain calibration, using 3C 286. First, we run the task `gaincal` to perform the delay calibration, using the entire bandwidth. We then carried out a time-dependent gain calibration using again `gaincal`, but just over a small part of RFI-free band to minimize any frequency dependence. After applying the delay and time dependent gain solution on-the-fly, we estimated frequency dependent gain solutions using the task `bandpass`. After these initial calibration steps, we did automated flagging using the `tfcrop` and `rflag` tasks on the residual visibilities to remove any low-level RFI, and repeated the previous calibration steps. After three rounds of calibration

and flagging, we found that the residual visibilities of 3C 286 looked clean. We finally applied the calibration solutions of the final round to our target, GJ 486. We then performed one round of automated flagging using `tfcrop` and `rflag` on the corrected visibilities of the target field. Since the central square antennas of the uGMRT have strong correlated RFIs, we performed this automated flagging step on the central square baselines and other baselines, separately.

We performed the imaging and self-calibration of our calibrated data with a modified version of the CAPTURE (CASA Pipeline-cum-Toolkit for Upgraded Giant Metrewave Radio Telescope data REduction) package (Kale & Ishwara-Chandra 2021). Since we needed to obtain both Stokes I and V products for our science purposes, we modified the pipeline scripts. In particular, since CAPTURE only uses the Stokes I model for self-calibration, which is not suitable for Stokes I and V imaging, we made separate RR and LL models and used them during the self-calibration steps. We could perform self-calibration since there were several compact and bright enough sources on the field of view. We first carried out four rounds of phase-only self-calibration with solution intervals of 8, 4, 2, and 1 min, followed by another four rounds of amplitude and phase calibration, using solution intervals of 4, 2, and 1 min for the last two rounds, to obtain the final image at each observing epoch.

We computed the dynamic spectra using the `dftdynamicspec` function from the `pwkit`<sup>1</sup> package (Williams et al. 2017). This function yields the dynamic spectrum of a point source by applying a discrete Fourier transform to its visibilities. Subsequently, we rebinned the dynamic spectra into frequency bins of 0.4 MHz to explore the presence of faint structures that might remain undetected with the native channel width (97.7 kHz).

## 4. Results

We summarize our main results in Table 2 and Figs. 2 and 3 (with additional information in Figure D.1). The main outcome is the non-detection of any steady radio emission above  $3\sigma$  level, where  $\sigma$  is the rms noise of the image, in any of our observing epochs, neither in Stokes I, nor in Stokes V, at the position of GJ 486 (Table 2 and Fig. 2). We calculated the image rms within a 60 arcsecond-wide squared region centered on the position of GJ 486 (green square in Fig. 2). The rms value in the images varied from epoch to epoch, ranging from 17.6 to 39.4  $\mu$ Jy/b and from 9.9 to 15.2  $\mu$ Jy/b in Stokes I and V, respectively. Note that the rms in the Stokes V images is significantly smaller than in the Stokes I images, as the field is essentially depleted of sources emitting in Stokes V, unlike in Stokes I. We also generated an image combining all the observing epochs, which also yielded non-detections. The rms of the stacked image is 16.7  $\mu$ Jy/b and 8.7  $\mu$ Jy/b for Stokes I and V, respectively.

The rms values in Table 2, and the images in Fig. 2, correspond to the averages over the entire observing epoch, both in time and frequency. Hence, it could be possible that our observations might have missed relatively bright, very short radio emission flares whose signal could have been washed out by averaging the data. We therefore obtained the dynamic spectra for all our observing epochs, both in Stokes I and V. The dynamic spectra confirmed that there was no bursting radio emission in any of our observing epochs. As an illustration, we show in Fig. 3 the dynamic spectra for our observations on 30 October 2021.

While the dynamic spectrum of the Stokes I data seems to show some structure on the emission, the dynamic spectrum of

<sup>1</sup> Available at <https://github.com/pkgw/pwkit>

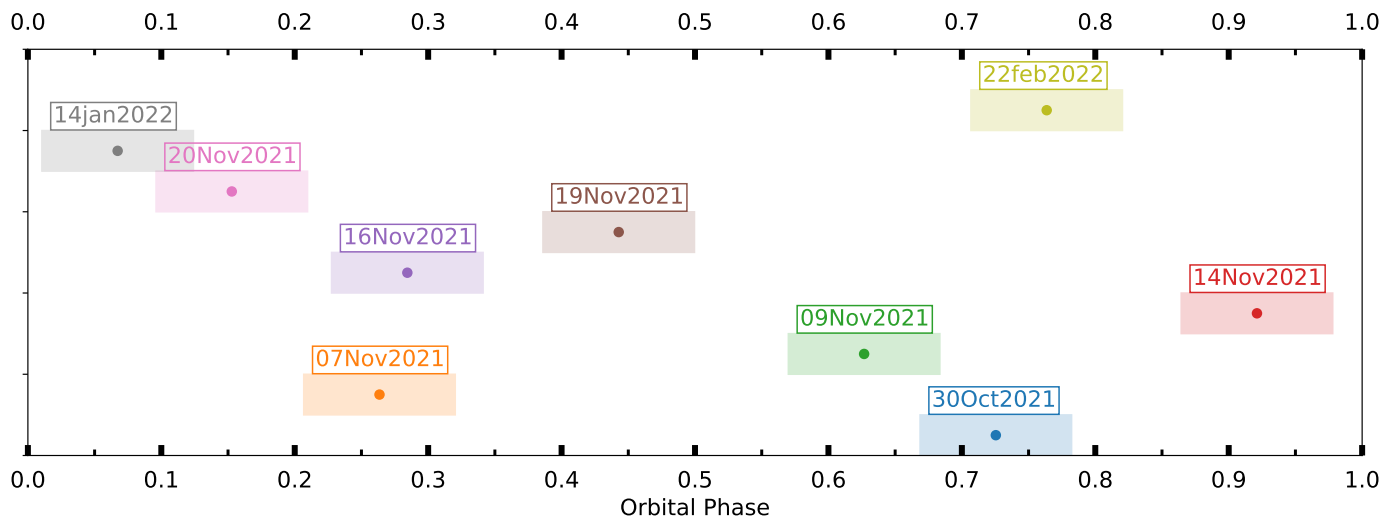


Fig. 1: Coverage of our uGMRT observations of the GJ 486 system, folded to the orbital period of GJ 486b of 1.47 d. Each epoch is shown with a different color. Each point corresponds to the central time of each observing epoch, with the horizontal side of the surrounding rectangle being the time span of the epoch. The vertical axis has no real meaning and the epochs are simply offset so they do not overlap.

Table 2: Observing log of the uGMRT observations of GJ 486 showing the value of local RMS in a region of  $60 \times 60$  arcsecond centered on the source ( $\sigma$ ).

Observation date YYYY-MM-DD	Start time HH:MM:SS.S	End time HH:MM:SS.S	$\sigma_I$ ( $\mu\text{Jy/b}$ )	$\sigma_V$ ( $\mu\text{Jy/b}$ )	bmaj (arcsec)	bmin (arcsec)	PA (deg)
2021-10-30	01:27:45.5	04:29:02.5	23.2	12.5	6.7	4.1	-60.9
2021-11-07	04:02:54.9	07:52:31.0	22.2	13.0	4.8	3.6	30.4
2021-11-09	03:22:12.1	07:33:38.2	18.5	11.6	4.8	3.5	43.8
2021-11-14	23:54:20.5	03:30:20.6 <sup>+1</sup>	13.0	9.9	5.4	3.9	69.7
2021-11-17	00:00:34.4	03:32:59.7	22.6	11.5	5.9	3.7	61.1
2021-11-19	03:43:01.6	07:31:11.8	22.9	14.6	4.3	3.6	20.71
2021-11-20	04:30:51.6	08:27:37.2	22.5	10.5	5.3	3.9	56.9
2022-01-14	19:50:15.4	23:56:08.6	31.5	10.9	5.2	3.8	-86.1
2022-02-23	00:52:28.6	03:48:34.2	17.7	12.1	7.9	3.8	68.7

**Notes.** The “+1” indicates that the observations starting on 2021-11-14 ended the next day.

the Stokes V shows no signal across the entire frequency and time domain, indicating that, even if the features seen in the Stokes I dynamic spectrum were real, their signals were not circularly polarized, and therefore were not of an electron cyclotron maser origin. Most likely, the apparent structure in the Stokes I data is due to artifacts and/or sidelobe contributions from other sources that were not perfectly removed from the field after the  $uv$ -subtraction. We show in Fig. D.1 the rest of the Stokes V dynamic spectra. As mentioned above, there is no sign of bursting emission in Stokes V, except for a single possible burst in the 20 November, which is due to an instrumental effect (see Appendix D for details).

## 5. Discussion

We discuss here the reasons that could have led to the non-detection of radio emission from magnetic star-planet interaction between GJ 486b and its host star, GJ 486, and its implications for the physical and geometrical parameters of the system. First, ECM emission is intrinsically time variable, so it is possible that nature did conspire against detecting it during our observations. However, our essentially full coverage of all orbital phases of GJ 486 makes this very unlikely. We also note that since our ob-

serving campaign took place over several months, we cannot rule out that we could have missed bursting emissions between two observing epochs related to, e.g., coronal mass ejections (CMEs) impacting the planet. Second, we cannot exclude completely the possibility that the ECM fundamental frequency fell down below our observing frequency. In fact, since the relevant magnetic field for ECM emission is the local magnetic field, if the emission took place at a significant height above the surface of the star, the field may have been significantly smaller than the one initially estimated, and our observing frequency may have been too high to detect the emission at the fundamental frequency. We notice that although emission at the second harmonic could have been potentially detected by our observations, it is generally less intense than emission at the fundamental frequency, and rarely observed (Melrose & Dulk 1982).

In the remaining of this section, we discuss the implications of the non-detections due to a too low intensity of the radio emission, and/or to anisotropic radio beaming toward directions different from the observer’s one. We address the former case by using a simple model to estimate the radio emission expected to arise from the (sub-Alfvénic) magnetic interaction between the star and its planet, which sets constraints on the stellar wind density at the orbit of GJ 486b, and on its planetary magnetic field



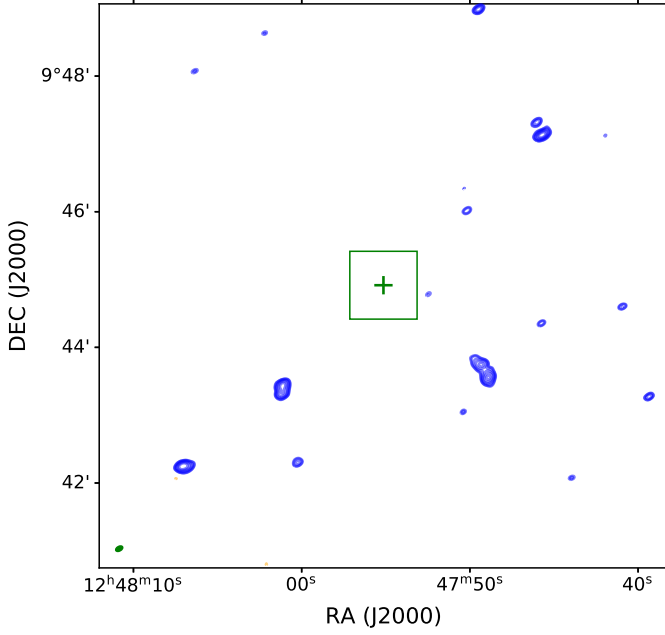


Fig. 2: Stokes I wide-field image centered on GJ 486 from band 4 (central frequency of 648 MHz) uGMRT observations on 30 October 2021. The image covers a region of  $\sim 8' \times 8'$ , centered at the position of GJ 486 (green cross). The synthesised beam is shown as a green solid ellipse on the bottom left. The green square corresponds to a region of  $60 \times 60$  arcsec squared, which we have used to estimate the local rms.

5.1. We address the latter scenario (anisotropic radio beaming) using the MASER code (Kavanagh & Vedantham 2023) to constrain the geometry of the system. MASER predicts the visibility of radio emission induced on a star via magnetic star-planet interaction, as a function of time (Sect. 5.3).

#### 5.1. Modelling the planet-induced radio emission from sub-Alfvénic interaction in GJ 486 – GJ 486b

If a planet is in the sub-Alfvénic regime ( $M_A = v/v_A < 1$ ), energy can be transported upstream back to the star along the stellar magnetic field line connecting to the planet (Saur et al. 2013). The key aspect, from an observational viewpoint, is that if this energy is dissipated via the ECM instability, the frequency of the emission should lie in the range of  $\sim 100$  MHz to GHz, as the relevant magnetic field is that of the  $B_*$ , which for M-dwarfs manifest with strengths ranging from  $\sim 10$  G upwards to 1 kG (Morin et al. 2008, 2010; Lehmann et al. 2024), which correspond to cyclotron frequencies in the above range.

The energy powering the observed ECM (radio) emission comes from the Poynting flux,  $S_{\text{Poynt}}$ , generated at the orbit of the planet. More specifically,  $S_{\text{Poynt}} \propto R_{\text{eff}}^2 v_{\text{rel}} B_{\perp}^2$ , where  $R_{\text{eff}}$  is the effective radius of the planet, given by Eq. 4 below (Zarka et al. 2001; Zarka 2007) (or equal to the planet radius if the planet is not magnetized);  $v_{\text{rel}}$  is the relative velocity between the stellar wind flow and the planet; and  $B_{\perp}$  is the component of the stellar wind magnetic field, perpendicular to the plasma velocity at the location of the planet.

The total radio power emitted from one hemisphere of the star is  $P_R = \beta S_{\text{Poynt}}$ , where  $\beta$  corresponds to the efficiency factor in converging Poynting flux to ECM radio emission. The value of  $\beta$  is not known, but is expected to be in the range from 0.0001 to

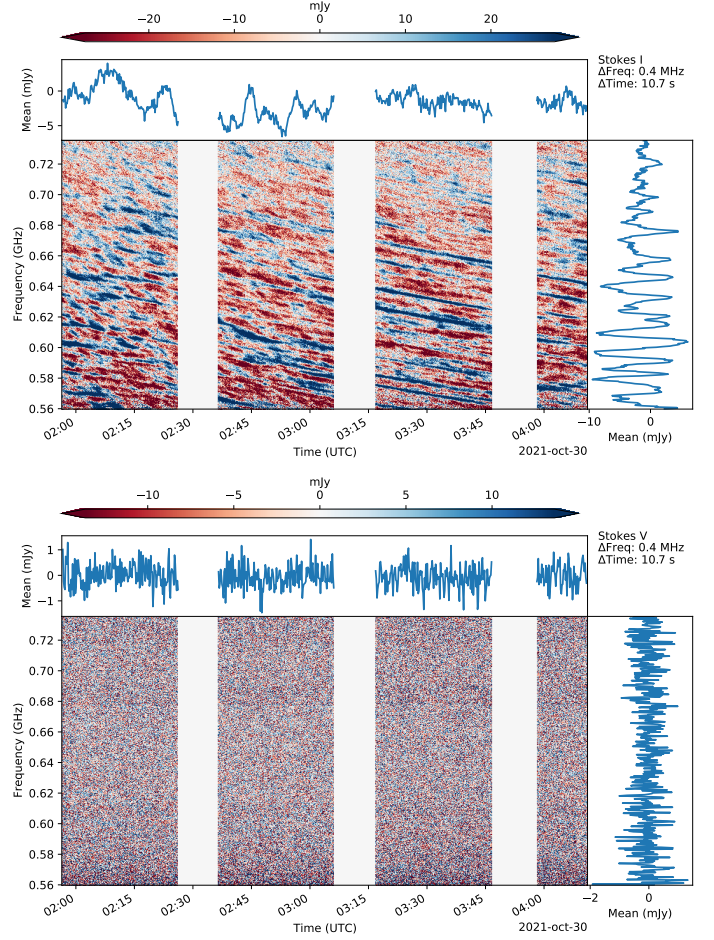


Fig. 3: Dynamic spectrum of the Stokes I and V (upper and lower panels, respectively) emission from the GJ 486 – GJ 486b system for our 30 October 2021 uGMRT observations in band 4, averaged in frequency ( $\Delta \nu = 0.4$  MHz). The time interval used is 10.7 s (which is the integration time). There is no apparent detection of radio emission above the noise. Blank regions correspond to times when we observed the phase calibrator. The spectra at the top and right of the dynamic spectrum result from collapsing all channels (top) and times (right). For a box located on time range 2:00 to 2:20 and frequency range 0.68 to 0.72 GHz, the rms values are 13.5 and 8.4 mJy for the Stokes I and V spectra, respectively.

0.01 for the planets of the Solar System (Zarka 2018, 2024). The radio flux density coming from the star can then be expressed as

$$F_R = \frac{P_R}{\Omega D^2 \Delta \nu}, \quad (2)$$

where  $\Omega$  is the solid angle into which the ECM radio emission is beamed,  $D$  is the distance to the star from Earth, and  $\Delta \nu$  is the total bandwidth of the ECM emission. Observations of the Io-DAM emission indicate that the beaming solid angle of a single flux tube is of about 0.16 sr (Kaiser et al. 2000; Queinnec & Zarka 2001). However, various reasons can lead to a larger solid beam of about a few times that value, e.g., a thick emission cone wall, a planetary plasma wake, or a distorted stellar magnetic field. On the other hand, there is no reason to consider a full auroral oval around the star, which in the case of Jupiter yields a beam solid angle of 1.6 sr (see, e.g., Zarka et al. 2004). We therefore used a value of  $\Omega = 0.5$  sr in our simulations, corresponding to a few times the size of a single magnetic flux tube.

We make the standard assumption that ECM radio emission has  $\Delta\nu = \nu_g$ , where  $\nu_g \approx 2.8 B_\star$  MHz is the cyclotron frequency, and  $B_\star$  is the average surface magnetic field strength of the star.

We follow the prescriptions in Appendix B of Pérez-Torres et al. (2021) to estimate the observed radio emission arising from the sub-Alfvénic star-planet interaction in the GJ 486–GJ 486b system, and consider a closed dipolar geometry for the stellar magnetic field. We compute the predicted radio emission using the Zarka/Saur/Turpenney model<sup>2</sup>

We approximate the stellar wind of GJ 486 as an isothermal, fully ionized, hydrogen plasma (Parker 1958), which is characterized by the sound speed, or equivalently, the coronal temperature,  $T_c$ . We use  $\log T_c = 6.67^{+0.40}_{-0.09}$  for GJ 486 from the work by Sanz-Forcada et al. (2024), who utilized XMM-Newton X-ray data to determine coronal temperatures for 21 CARMENES stars.

The stellar wind density ( $\rho_{sw}$ ) at the orbit of GJ 486 b is not known beforehand. We therefore parameterize it via the stellar mass-loss rate,  $\dot{M}_\star$ :

$$\rho_{sw} = \frac{\dot{M}_\star}{4\pi d^2 v_{sw}}, \quad (3)$$

which follows from the mass conservation equation for a time-independent stellar wind with constant  $\dot{M}_\star$ . Here,  $d$  is the semi-major axis of the orbit of the planet (see Table 1), and  $v_{sw}$  is the stellar wind speed at the planet position. The stellar wind number density is  $n_{sw} = \rho_{sw}/\mu m_p$  and, since we assume a fully ionized, purely hydrogen plasma,  $\mu = 1/2$ .

The main difference with respect to the modeling in Pérez-Torres et al. (2021) is that here we also take into account the effect of free-free absorption. While for the nominal value of  $T_c$  its impact is negligible, for the lower limit it can significantly impact the amount of transmitted radio-signal, if the stellar wind mass-loss rate is very high (see Fig. 4). We show the modeling of this effect in appendix B.

The effective obstacle radius of the planet is given by the magnetopause standoff distance of the planet,  $R_{mp}$ , which we obtain by assuming a pressure balance between the stellar wind pressure (dynamic, thermal, and magnetic pressures) and the planetary pressure (magnetic pressure):

$$R_{mp} = k_{mp}^{1/3} \left[ \frac{(B_{pl}/2)^2/8\pi}{p_{dyn,sw} + p_{th,sw} + B_{sw}^2/8\pi} \right]^{1/6} R_{pl}, \quad (4)$$

where  $k_{mp}$  is the factor by which the magnetopause currents enhance the magnetospheric magnetic field at the magnetopause, which is a value between 2 and 3. For simplicity, we adopt here  $k_{mp} = 2$ .  $B_{pl}$  is the intensity of the (dipolar) planetary magnetic field at the poles,  $p_{dyn,sw} = \rho v_{rel}^2$  and  $p_{th,sw} = n_{sw} k_B T_c$  are the dynamic and thermal components of the stellar wind pressure, respectively;  $B_{sw}$  is the magnetic field intensity of the stellar wind, and  $R_{pl}$  is the planetary radius. We note that Eq. 4 is an approximation to the actual value of the magnetopause standoff distance,

<sup>2</sup> We note that in a number of previous works (e.g., Vedantham et al. 2020, Mahadevan et al. 2021, Pérez-Torres et al. 2021), those models had been dubbed Zarka and Saur/Turpenney, since they were thought to predict significantly different levels of radio emission. However, during the Lorentz workshop ‘‘The life cycle of a radio star’’, held in Leiden, this issue was discussed and it was found that those models predict essentially the same flux densities, within about a factor of two (Callingham et al. 2024; Zarka 2024).

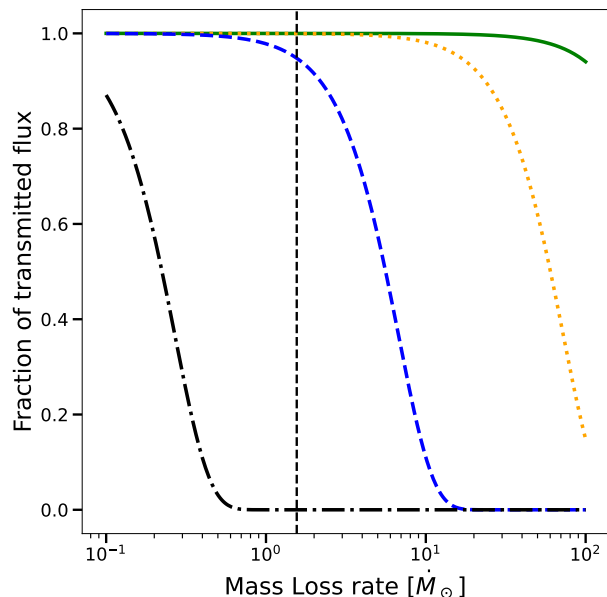


Fig. 4: Fraction of transmitted SPI flux due to the effect of free-free absorption for  $T_c$  values of 1 (dot-dashed black line), 1.5 (blue dashed line), 2.5 (orange dotted line) and 4.7 (green solid line) MK.

and does not take into account effects such as the topology or the reconnection of the interplanetary magnetic field (IMF) with the magnetic field of the planet. For instance, the tilt of the magnetic field of the planet with respect to the IMF can increase the value of  $R_{mp}$  for a Proxima b-like planet by a factor of up to seven (Peña-Moñino et al. 2024).

Finally, we estimated the magnetic field of the planet using the Sano’s scaling law (Sano 1993). This resulted in a value of  $B_{pl} \simeq 0.85$  G (see A), around 40% larger than the magnetic field of the Earth at the poles. We show in Fig. 5 the effective radius and magnetopause standoff distance as a function of the magnetic field of the planet. If  $B_{pl} \lesssim 0.35$  G, then the effective radius is that of the planet itself. For  $B_{pl} = 0.85$  G, the nominal value of the magnetic field, the effective radius is about 40% larger than the physical radius of the planet.

## 5.2. Constraints from the modeling of the radio emission

In this section, we use the modeling described in Sect. 5.1 to constrain some of the physical parameters of the system, in the case that the non-detections were due to the signal being too low to be detectable. We show in Fig. 6 the predicted radio emission arising from the sub-Alfvénic star-planet interaction in the GJ 486–GJ 486b system, as a function of  $\dot{M}_\star$  and  $B_{pl}$  for two different values of the coronal temperature of GJ 486:  $T_c = 10^{6.67} = 4.7$  MK (top), corresponding to the nominal value; and  $T_c = 10^{6.40} = 2.5$  MK (bottom), corresponding to the 3- $\sigma$  lower limit of the coronal temperature determined by Sanz-Forcada et al. (2024). Left panels correspond to the case of an unmagnetized planet, while middle ones correspond to the case of a planet with  $B_{pl} = 0.85$  G, the nominal estimated magnetic field value of GJ 486b (see Appendix A).

The vertical lines in the plots correspond to the nominal value of  $\dot{M}_\star = 1.4 \dot{M}_\odot$ , obtained by applying Eq. 7 in Johnstone et al. (2015) to the GJ 486 star, and using the values in Table 1.

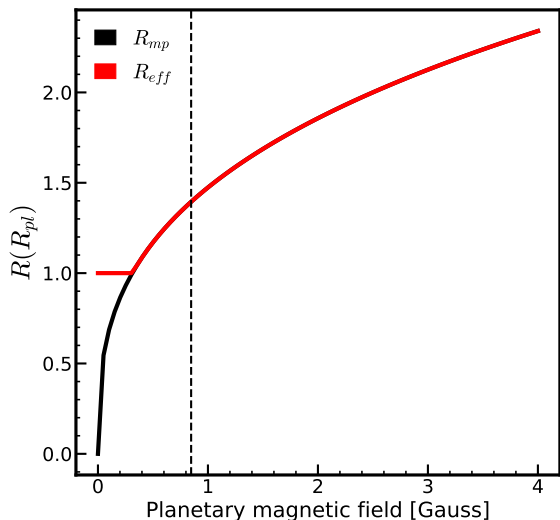


Fig. 5: Magnetopause standoff distance,  $R_{mp}$ , and effective radius,  $R_{eff}$ , as a function of the magnetic field of the planet,  $B_{pl}$ . If  $B_{pl} \geq 0.35$  G,  $R_{eff} = R_{mp}$ , otherwise  $R_{eff} = R_{pl}$ . The vertical dashed line corresponds to the nominal value of the magnetic field of 0.85 G.

Our predictions already take into account that the efficiency of the conversion of Poynting flux into radio emission,  $\beta$ , is poorly known, but is very unlikely to be above 1%, and possibly closer to 0.2% or even lower Zarka (2024). This results in the yellow (cross-hatched) areas in the plots of Fig. 6, which correspond to the expected radio flux density including (neglecting) free-free absorption from the thermal electrons in the stellar wind.

The majority of M dwarfs have winds that are weaker than, or comparable to, that of the sun, i.e.,  $\dot{M}_* \lesssim \dot{M}_\odot$  (Wood et al. 2021;  $\dot{M}_\odot = 2 \times 10^{-14} M_\odot \text{ yr}^{-1}$ ). However, Wood et al. (2021) found in their sample that two M dwarfs showed values of  $\dot{M}_* = 30 \dot{M}_\odot$  (YZ CMi, M4 Ve) and  $\dot{M}_* = 10 \dot{M}_\odot$  (GJ 15AB; M2 V + M3.5 V). Therefore, in our study of the SPI radio-signal as a function of the stellar density, and given our lack of knowledge of the stellar mass loss rate of GJ 486, we used values of  $\dot{M}_*$  in the range from 0.1 up to  $100 \dot{M}_\odot$ . This broad range encompasses the whole range of values inferred for M dwarfs to date (Wood et al. 2021).

Our reference case is the one shown in the top middle panel of Fig. 6, i.e., a magnetized planet with  $B_{pl} = 0.85$  G orbiting its host star GJ 486, which has  $T_c = 4.7$  MK. The planet is in the Sub-Alfvénic regime as long as  $\dot{M}_* \lesssim 57 \dot{M}_\odot$ , so the planet-induced Poynting flux can be transferred to the star and be re-emitted as auroral ECM emission at radio wavelengths. If the stellar wind mass-loss rate were higher, the planet would be always in a Super-Alfvénic regime, and there would be no emission arising from SPI. However, given the inferred value of  $\dot{M}_*$  for GJ 486, it is very unlikely that such mass-loss rates are at place. Since the (nominal) value of  $T_c$  is large, free-free absorption effects (yellow areas in the plots) are negligible, regardless of the value of  $\dot{M}_*$ . For the nominal value of  $\dot{M}_* = 1.4 \dot{M}_\odot$ , we should have clearly detected radio emission from SPI, independently of the value of  $\beta$ . Only if  $\dot{M}_*$  is much smaller than  $\dot{M}_\odot$  ( $\dot{M}_* \lesssim 0.3 \dot{M}_\odot$ ) and if, at the same time,  $\beta \ll 0.01$ , could we have expected a non-detection. If the planet is not magnetized (top left panel), non-detections could be expected for values  $\dot{M}_* \lesssim 1.2 \dot{M}_\odot$ , but also requiring small values of  $\beta$ . The top right

panel also shows that, for the nominal value of  $T_c$ , we should have detected radio emission from SPI, whether the planet is magnetized or not, unless  $\beta \lesssim 10^{-3}$ . The bottom panels show the same set of simulations as in the top panels, but for  $T_c = 2.5$  MK. The main differences with respect to the case of  $T_c = 4.7$  MK, are the following: the planet enters the super-Alfvénic regime at much larger values of  $\dot{M}_* (\gtrsim 91 \dot{M}_\odot)$ ; the predicted flux is about a factor of two smaller; free-free absorption effects are noticeable, since  $T_c$  is lower, albeit only for large values of  $\dot{M}_*$ . The strong lower limit on  $T_c$  would have implied a detection of radio emission from SPI, if  $\dot{M}_* \gtrsim 1.2 \dot{M}_\odot (\gtrsim 4.7 \dot{M}_\odot)$  for a magnetized (non-magnetized) planet, irrespective of the value of  $\beta$ . As in our reference case, non-detections imply not only very small values of  $\dot{M}_*$ , but also that simultaneously the efficiency in converting Poynting flux into SPI radio emission is quite low ( $\beta \ll 0.01$ ). The bottom right panel shows essentially the same results as in the top right panel, i.e., that independently of whether the planet is magnetized, or not, we should have expected a detection of radio emission from SPI unless  $\beta \lesssim 10^{-3}$ .

Summarizing, if the non-detection of radio emission from SPI in GJ 486 was due to an intrinsically dim signal, this suggests that, independently of whether the planet is magnetized or not, the mass-loss rate must have been small ( $\dot{M}_* \lesssim 0.3 \dot{M}_\odot$ ) and that, concomitantly, the efficiency of the conversion of Poynting flux into radio emission was low, with values of  $\beta$  close to 0.001, or even lower. If the value of  $\beta$  had been higher, then detections would have been warranted, regardless of the values of  $B_{pl}$  and  $\dot{M}_*$ .

### 5.3. Constraints on the geometry of the system

In the previous section, we discussed the constraints that can be inferred from modelling the radio emission, as described in Sect. 5.1, if the absence of a radio detection was due to the ECM signal being too faint to be detectable. Here we discuss an alternative scenario. Namely, that the signal might have been strong enough, but that our lack of knowledge about the stellar rotation, magnetic field geometry, and/or orbital and emission cone geometry could have resulted in the emission being beamed out of the line of sight during our observations.

We used the MASER code developed by Kavanagh & Vedantham (2023) to determine whether this was the case. MASER takes in all key parameters pertaining to the geometry of the stellar rotation, stellar magnetic field, planetary orbit, and emission cone<sup>3</sup>, and determines whether radio emission generated along the magnetic field line connecting the star to the planet is visible to the observer as a function of time (called a visibility lightcurve). We first constructed uninformed prior distributions for each parameter, which we list in Table 3. From each distribution, we drew one million samples for each parameter, and computed the visibility lightcurve of the system during the observing windows listed in Table 2. (Note that we divided up each window into 100 points.) We then constructed a probability density for each parameter from the sets of samples that produced lightcurves with zero visibility. If any deviated from the assumed prior distribu-

<sup>3</sup> The MASER code assumes the emission cone properties are independent of the emission frequency. However, other existing codes such as EXPRES (Hess & Zarka 2011; Louis et al. 2019) prescribe these properties based on the emission frequency, field strength, and velocity of the electrons powering the ECM emission. This however is informed by in-situ observations from Jupiter, which we lack in the case of GJ 486. Therefore, we opt to use MASER, which is also optimized for parallelized exploration of parameter spaces.



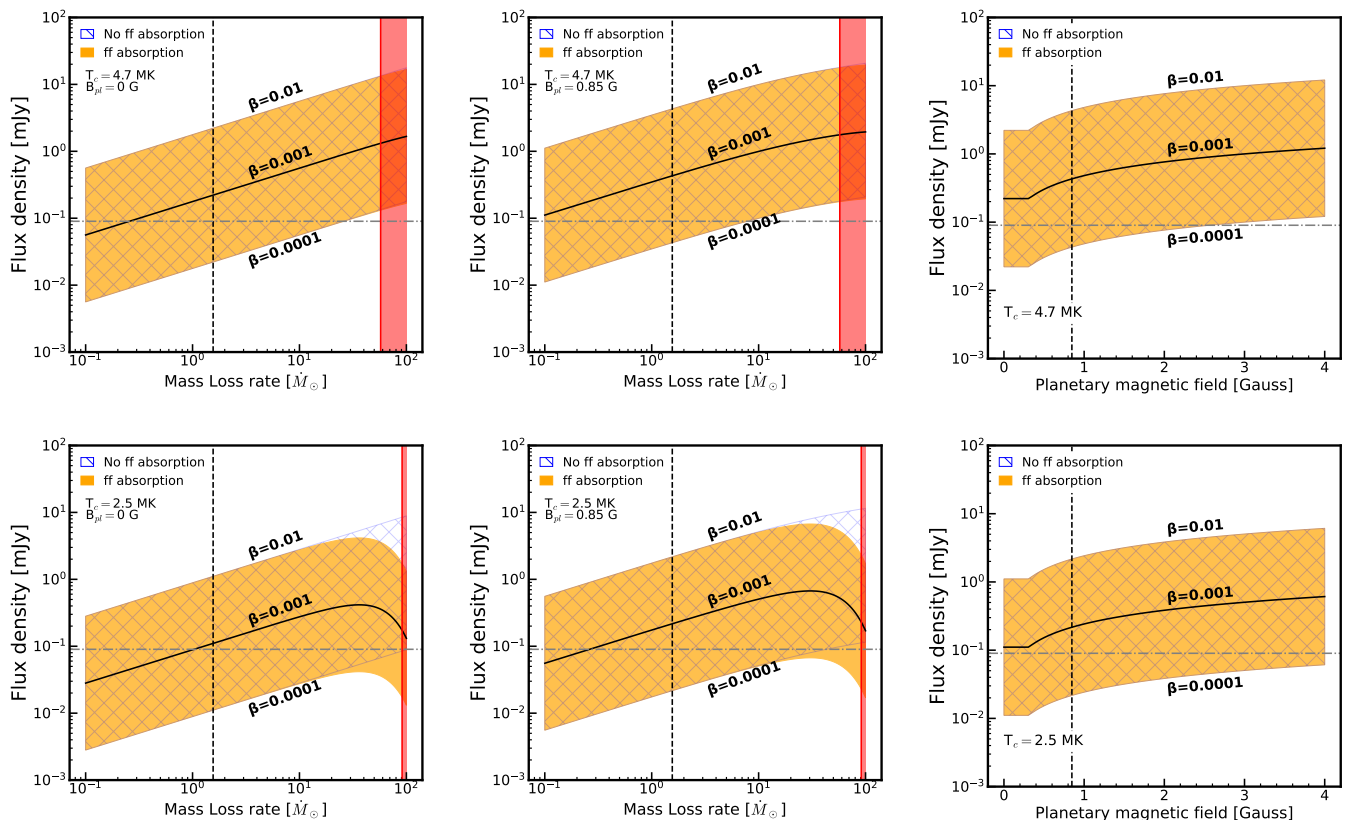


Fig. 6: Predicted flux density arising at a nominal frequency of 670 MHz from star planet interaction. The yellow (cross-hatched) areas correspond to the expected radio flux density, including (neglecting) free-free absorption from the thermal electrons in the stellar wind. The rows correspond to the expected emission for two different values of the coronal temperature,  $T_c = 4.7$  MK (the nominal value; top row) and  $T_c = 2.5$  MK ( $3\text{-}\sigma$  lower limit; bottom row). The left and middle panels show the predicted flux density as a function of the stellar wind mass-loss rate for an unmagnetized planet (left) and a magnetized one with  $B_{\text{pl}} = 0.85$  G (middle), with a vertical dashed line showing the nominal value,  $\dot{M}_* = 1.4 \dot{M}_\odot$  (see text for details). The right panels show the predicted flux density as a function of the planetary magnetic field, for the aforementioned nominal value of  $\dot{M}_*$ , and a vertical dashed line corresponding to the nominal value of the magnetic field,  $B_{\text{pl}} = 0.85$  G. Red areas correspond to values  $M_A \geq 1$ , i.e., where the planet is in the Super-Alfvénic regime, therefore model predictions are not valid. The horizontal dash-dotted lines correspond to the  $3\sigma$  detection threshold of our observations (where  $\sigma = 30 \mu\text{Jy b}^{-1}$ ).

tion, this implied that certain values for the parameter were more probable for the system.

Kavanagh & Vedantham (2023) found that certain configurations for the stellar rotation and magnetic axis produce emission that is visible for a large percentage of time. These configurations describe systems where the magnetic axis of the star is always inclined relative to the observer by the cone opening angle,  $\alpha$  (see Fig. 2 in Kavanagh & Vedantham 2023). In the case of GJ 486 we find, however, the opposite. In Figure 7 we show a 2D probability density of the magnetic obliquity against the stellar inclination for systems with no visible emission. We see a pattern that is effectively the opposite of what is shown in Figure 8 of Kavanagh & Vedantham (2023), i.e. configurations where the magnetic axis never forms the angle  $\alpha$  with the line of sight. Note that in Fig. 7, the darker the color, the more likely is to have a non-detection of SPI in the GJ 486 system (assuming SPI is in action in the system and we have the sensitivity to detect it). We highlight the three most probable configurations for a non-detection of SPI, denoted # 1, # 2 and # 3. We show in Figure 8 a sketch of the first possible configuration (# 1). The region describes a configuration where the system is viewed edge-on, with a low magnetic obliquity. For completeness, we have also included to-scale sketches of the additional two most probable

configurations inferred, # 2 and # 3, and show them in appendix C. Those findings illustrate how non-detections of magnetic star-planet interactions can also be informative when combined with numerical models such as MASER.

## 6. Summary and outlook

We have presented the results of the longest radio monitoring campaign on the GJ 486 - GJ 486b system, whose star hosts an Earth-like, rocky planet, aimed at finding evidence of radio emission arising from magnetic star-planet interaction. We observed GJ 486 with the upgraded Giant Metrewave Radio Telescope (uGMRT) in the frequency range from 550 to 750 MHz (where we expected the cyclotron emission to take place, since this covers a surface magnetic field ranging from 196 to 268 G) in nine different epochs, between 30 October 2021 and 22 February 2022, covering almost all orbital phases of GJ 486b.

We obtained radio images of the region around GJ 486, both in Stokes I (total intensity) and V (circularly polarized intensity). We did not detect any quiescent radio emission in any epoch above a  $3\sigma$  noise floor of (33–96)  $\mu\text{Jy/b}$  and (30–45)  $\mu\text{Jy/b}$  Stokes I and Stokes V images, respectively. We obtained dynamic spectra in both Stokes I and V for all individual epochs, but did not find any evidence of short, bursty activity either. Our



Table 3: List of unconstrained (or poorly constrained) relevant parameters of the GJ 486 system used in our MASER simulations.

Parameter	Prior distribution	Units
Stellar rotation period ( $P_{\text{rot}}$ )	$\mathcal{N}(49.9, 5.5)$	days
Cosine of stellar inclination ( $\cos i_*$ )	$\mathcal{U}(0, 1)$	–
Stellar rotation phase at start of observations ( $\phi_{*,0}$ )	$\mathcal{U}(0, 1)$	–
Dipole field strength of the stellar magnetic field ( $B_*$ )	$\mathcal{U}(100, 1000)$	Gauss
Magnetic obliquity of the stellar magnetic field ( $\beta$ )	$\mathcal{U}(0, 90)$	degrees
Projected spin-orbit angle ( $\lambda$ )	$\mathcal{U}(0, 360)$	degrees

**Notes.** For the prior distributions, we either use a normal ( $\mathcal{N}$ ) or uniform ( $\mathcal{U}$ ) distribution. For the normal distribution, the values in brackets are the center and standard deviation, and for the uniform distribution, the values are the minimum and maximum of the distribution. Note that we uniformly sample the cosine of the stellar inclination, which uniformly scatters the rotation axis on the surface of a sphere (see [Kavanagh & Vedantham 2023](#)). We fix the cone opening angle  $\alpha$  to  $75^\circ$  and the cone thickness  $\Delta\alpha$  to  $1^\circ$  in our simulation. Note also that extending the values for  $i_*$  and  $\beta$  beyond  $90^\circ$  produces symmetric results of those shown in Figure 7

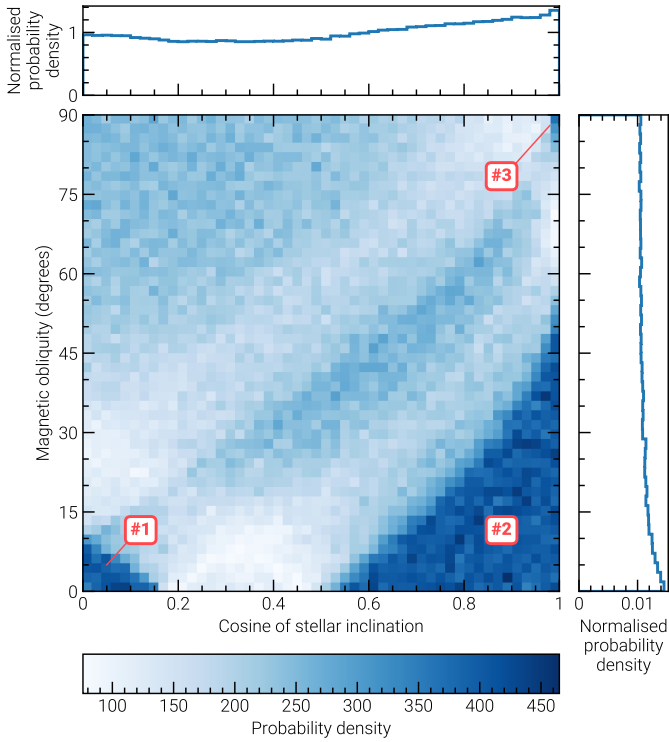


Fig. 7: Probability density for the stellar inclination and magnetic obliquity of GJ 486 given the non-detection of magnetic star-planet interactions. The darker blue colour corresponds to a higher probability of non-detection. The top and right panel shows the 1-dimensional histogram for each parameter. Note that this assumes that magnetic star-planet interactions take place in the system and we have the sensitivity to detect them (see main text for details).

non-detections could have been due to four reasons: (1) time variability of the emission; (2) a different frequency range than the one we observed at; (3) an SPI radio signal too low to be detectable; and (4) the anisotropic radio beaming pointing to a direction away from the observer.

(1) Since we obtained an almost full coverage of the orbital phases of GJ 486b, and the resulting dynamic spectra showed no bursting signal at any time, it seems extremely unlikely that we missed the signal because of the putative SPI signal being time variable. (2) The frequency range where we observed was

#1

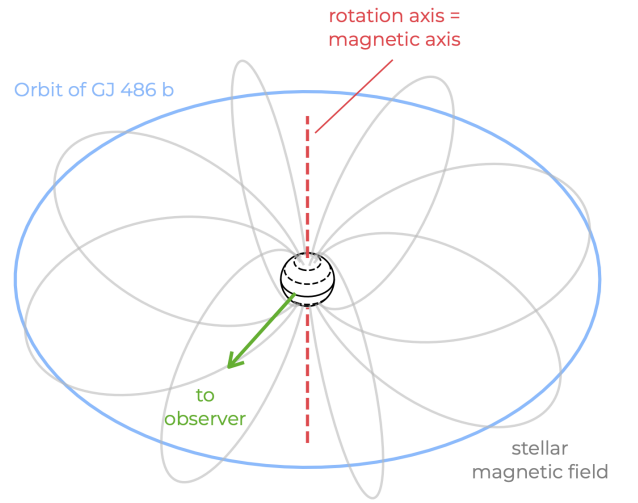


Fig. 8: To-scale sketch of the geometry for case #1, inferred for the GJ 486 planetary system based on our non-detection of star-planet interactions at radio wavelengths. The system is viewed equator-on, and has a low magnetic obliquity, meaning the magnetic dipole is aligned with the rotation axis (shown as a dot on the surface). The orbit of GJ 486 b is shown in blue, and the stellar magnetic field line connecting to the orbit is shown in red. The dashed lines on the stellar surface are lines of constant latitude, with the solid line showing the equator. Note that we find no bias towards any projected spin-orbit angle  $\lambda$ . For simplicity, we set  $\lambda = 0^\circ$  here.

well tuned based on existing observations that indicate a magnetic field of about 240 G, although we cannot exclude that the maximum value of the cyclotron frequency fell below our lowest available frequency. This aspect suggests the need to either have beforehand stellar magnetic fields estimates from Zeeman Doppler Imaging (ZDI), or setting up simultaneous ZDI and radio observations.

We tackled the potential issue of (3) the SPI radio signal being too faint by modeling the energetics of star-planet interaction (Sect. 5.1 and 5.2). Our modeling strongly suggests that stellar wind mass-loss rate of GJ 486 must have been small ( $\dot{M}_* \lesssim$

$0.3 \dot{M}_{\odot}$ ), irrespective of whether the planet is magnetized, or not, and that, simultaneously, the efficiency of the conversion of Poynting flux into radio emission, is very low ( $\beta \lesssim 0.001$ ). If the value of  $\beta$  had been higher, then detections would have been warranted, regardless of the values of  $B_{\text{pl}}$  and  $\dot{M}_{\star}$ . We also note that free-free absorption effects are negligible, given the high value of the coronal temperature of the star ( $T_c = 4.7$  MK), and although they are noticeable above  $\dot{M}_{\star} \approx 20 \dot{M}_{\odot}$  for the strong lower limit of the coronal temperature of the star ( $T_c = 2.5$  MK), this should not have prevented the detection of radio emission from SPI.

Finally, we discussed the alternative possibility (4) that the SPI radio signal was strong enough to be detectable, but the anisotropic radio beaming could have been pointing to a direction away from our line of sight, so we could have missed it. To this end, we used the MASER code to constrain the geometry of the system. From our non-detections, we conclude that the magnetic obliquity and the stellar inclination are very low.

All of this illustrates how non-detections of magnetic star-planet interactions can also be informative when combined with a numerical modeling of both the energetic and the geometry of the system. We emphasize the need of accurate determinations of the magnetic field strength of M stars hosting planets, using e.g., the ZDI method. ZDI can also provide the stellar inclination and magnetic obliquity, and therefore would be an extremely useful tool to guide observing strategies at radio and other wavelengths. We also emphasize the need obtaining x-ray measurements of M dwarf stars to reliably determine their coronal temperatures, and assess the role of free-free absorption.

We end by noting that the detection of radio emission from star-planet interaction in M-dwarf systems hosting Earth-like exoplanets is proving to be very challenging, as the case of GJ 486 highlights, and the direct detection of small, Earth-like exoplanets would only be viable with hypothetical space-based instruments, like the FARSIDE initiative (Hallinan et al. 2021), among others. On the other hand, the detection of Jupiter-like planets from radio observations is more promising, as their magnetic fields are expected to be large enough as to have their associated gyrofrequency above the ionosphere cut-off, and the radio emission should be much larger than that from an Earth-like planet. However, the only potential detection is so far that of  $\tau$  Boo (Turner et al. 2021). While efforts at the extreme edge of low-frequencies ( $\nu \lesssim 50$  MHz), like NenuFAR, are worthwhile, current low-frequency ( $\nu \lesssim 100$  MHz) radio interferometers lack the necessary sensitivity and are affected by severe radio frequency interference to detect directly radio emission from Jupiter-like exoplanets, we may still need to wait for LOFAR 2.0 and SKA-low to be operational.

*Acknowledgements.* We thank the referee, Philippe Zarka, for his thorough and insightful review, which significantly improved our manuscript. We thank Sanne Bloor for her suggestion to take into account free-free absorption effects in our modelling of the radio emission. LPM, MPT, GB, JFG, JM, GA, AA, PA, DR, MO, and JAC acknowledge financial support through the Severo Ochoa grant CEX2021-001131-S, and through the Spanish National grants PID2023-147883NB-C21, PID2020-114461GB-I00, PID2023-146295NB-I00, and PID2022-137241NB-C42, all of them funded by MCIU/AEI/ 10.13039/501100011033, LPM also acknowledges funding through grant PRE2020-095421, funded by MCIU/AEI/10.13039/501100011033 and by FSE Investing in your future. We also acknowledge the service and support of the Spanish Prototype of an SRC (SPSRC), funded by the Spanish Ministry of Science, Innovation and Universities, by the Regional Government of Andalusia, by the European Regional Development Funds and by the European Union NextGenerationEU/PRTR. G.B-C acknowledges support from grant PRE2018-086111, funded by MCIN/AEI/ 10.13039/501100011033 and by 'ESF Investing in your future'

## References

- Anglada-Escudé, G., Amado, P. J., Barnes, J., et al. 2016, *Nature*, 536, 437
- Caballero, J. A., González-Álvarez, E., Brady, M., et al. 2022, *A&A*, 665, A120
- Callingham, J. R., Pope, B. J. S., Kavanagh, R. D., et al. 2024, *Nature Astronomy*, 8, 1359
- Cox, A. N. 2000, *Allen's astrophysical quantities* (Springer New York, NY)
- Gupta, Y., Ajithkumar, B., Kale, H. S., et al. 2017, *Current Science*, 113, 707
- Güdel, M., Schmitt, J. H. M. M., Bookbinder, J. A., & Fleming, T. A. 1993, *ApJ*, 415, 236
- Hallinan, G., Burns, J., Lux, J., et al. 2021, in *Bulletin of the American Astronomical Society*, Vol. 53, 379
- Hess, S. L. G. & Zarka, P. 2011, *A&A*, 531, A29
- Johnstone, C. P., Güdel, M., Lüftinger, T., Toth, G., & Brott, I. 2015, *A&A*, 577, A27
- Kaiser, M. L., Zarka, P., Kurth, W. S., Hospodarsky, G. B., & Gurnett, D. A. 2000, *J. Geophys. Res.*, 105, 16053
- Kale, R. & Ishwara-Chandra, C. H. 2021, *Experimental Astronomy*, 51, 95
- Kavanagh, R. D. & Vedantham, H. K. 2023, *MNRAS*, 524, 6267
- Kochukhov, O. 2021, *A&A Rev.*, 29, 1
- Lamy, L., Colomban, L., Zarka, P., et al. 2022, *Journal of Geophysical Research: Space Physics*, 127, e2021JA030160, e2021JA030160 2021JA030160
- Lehmann, L. T., Donati, J. F., Fouqué, P., et al. 2024, *MNRAS*, 527, 4330
- Louis, C. K., Hess, S. L. G., Ceconi, B., et al. 2019, *A&A*, 627, A30
- Mahadevan, S., Stefánsson, G., Robertson, P., et al. 2021, *The Astrophysical Journal Letters*, 919, L9
- McMullin, J. P., Waters, B., Schiebel, D., Young, W., & Golap, K. 2007, in *ASP Conference Series*, Vol. 376, *Astronomical Data Analysis Software and Systems XVI*, ed. R. A. Shaw, F. Hill, & D. J. Bell, 127
- Melrose, D. B. & Dulk, G. A. 1982, *ApJ*, 259, 844
- Morin, J., Donati, J. F., Petit, P., et al. 2008, *MNRAS*, 390, 567
- Morin, J., Donati, J. F., Petit, P., et al. 2010, *MNRAS*, 407, 2269
- Moutou, C., Hébrard, E. M., Morin, J., et al. 2017, *MNRAS*, 472, 4563
- Narang, M., Puravankara, M., Vedantham, H. K., et al. 2024, *The Astronomical Journal*, 168, 265
- Parker, E. N. 1958, *ApJ*, 128, 664
- Pérez-Torres, M., Gómez, J. F., Ortiz, J. L., et al. 2021, *A&A*, 645, A77
- Peña-Moñino, L., Pérez-Torres, M., Varela, J., & Zarka, P. 2024, *A&A*, 688, A138
- Pineda, J. S. & Villadsen, J. 2023, *Nat Astron*, 7, 569
- Queinnec, J. & Zarka, P. 2001, *Planet. Space Sci.*, 49, 365
- Quirrenbach, A., Amado, P. J., Caballero, J. A., et al. 2016, in *Ground-based and Airborne Instrumentation for Astronomy VI*, ed. C. J. Evans, L. Simard, & H. Takami, Vol. 9908, *International Society for Optics and Photonics (SPIE)*, 990812
- Reiners, A., Shulyak, D., Käpylä, P. J., et al. 2022, *A&A*, 662, A41
- Reylé, C., Jardine, K., Fouqué, P., et al. 2021, *A&A*, 650, A201
- Ribas, I., Reiners, A., Zechmeister, M., et al. 2023, *A&A*, 670, A139
- Ricker, G. R., Winn, J. N., Vanderspek, R., et al. 2014, *Journal of Astronomical Telescopes, Instruments, and Systems*, 1, 014003
- Sabotta, S., Schlexer, M., Chaturvedi, P., et al. 2021, *A&A*, 653, A114
- Sano, Y. 1993, *J. Geomag. Geoelectr.*, 45, 65
- Sanz-Forcada, J., López-Puertas, M., & Lampón, M. 2024, *A&A*
- Saur, J., Grambusch, T., Duling, S., Neubauer, F. M., & Simon, S. 2013, *A&A*, 552, A119
- Shulyak, D., Reiners, A., Nagel, E., et al. 2019, *A&A*, 626, A86
- Stelzer, B., Marino, A., Micela, G., López-Santiago, J., & Liefke, C. 2013, *MNRAS*, 431, 2063
- The CASA Team. 2022, *Publications of the Astronomical Society of the Pacific*, 134, 114501
- Trifonov, T., Caballero, J. A., Morales, J. C., et al. 2021, *Science*, 371, 1038
- Trigilio, C., Biswas, A., Leto, P., et al. 2023, *arXiv e-prints*, arXiv:2305.00809
- Turner, J. D., Zarka, P., Grießmeier, J.-M., et al. 2021, *A&A*, 645, A59
- Turnpenney, S., Nichols, J. D., Wynn, G. A., & Burleigh, M. R. 2018, *ApJ*, 854, 72
- Vedantham, H. K., Callingham, J. R., Shimwell, T. W., et al. 2020, *Nat Astron*, 4, 577
- Williams, P. K. G., Clavel, M., Newton, E., & Ryzhkov, D. 2017, *pwkit: Astronomical utilities in Python*, *Astrophysics Source Code Library*, record ascl:1704.001
- Wood, B. E., Müller, H.-R., Redfield, S., et al. 2021, *The Astrophysical Journal*, 915, 37
- Wu, C. S. & Lee, L. C. 1979, *ApJ*, 230, 621
- Zarka, P. 2007, *Planet. Space Sci.*, 55, 598
- Zarka, P. 2018, in *Handbook of Exoplanets*, ed. H. J. Deeg & J. A. Belmonte, 22
- Zarka, P. 2024, *arXiv e-prints*, arXiv:2409.16038
- Zarka, P., Ceconi, B., & Kurth, W. S. 2004, *JGR (Sp. Physics)*, 109, A09S15
- Zarka, P., Treumann, R. A., Ryabov, B. P., & Ryabov, V. B. 2001, *Ap&SS*, 277, 293

## Appendix A: Planetary magnetic field

Since the planet GJ 486b has a bulk density slightly larger, but close to being Earth-like, we estimated its magnetic field by assuming a Sano scaling law (Sano 1993), which is adequate for magnetized planets of the Solar System.

The magnetic field moment,  $\mathcal{M}$  is then  $\mathcal{M} \propto \rho_c^{1/2} \omega r_c^{7/2}$ . Here,  $\rho_c$  is the mass density in the dynamo region,  $\omega$  is the rotational speed of the planet, and  $r_c$  is the planet core radius, assumed to be  $\sim 0.55 R_{\text{pl}}$ , as in the case of the Earth. For simplicity, we assume  $\rho_c$  to be the planet bulk density, which we estimate by using the planetary mass and radius in Table 1. Since the rotational speed,  $\omega$ , of GJ 486b is unknown, we assume that GJ 486b is tidally locked, so that its rotational speed is equal to the orbital speed. The surface magnetic field of GJ 486b is then  $B_{\text{pl}} = \mathcal{M}/R_{\text{pl}}$ . Adopting  $B_{\oplus} = 0.5$  G, we get  $B_{\text{pl}} = 0.85$  G.

## Appendix B: Free-free absorption

Free-free absorption attenuates the radio signal by a factor of  $e^{-\tau_\nu}$ , where the optical depth,  $\tau_\nu$ , is defined as (Cox 2000)

$$\tau_\nu = \int_{R_\star}^{\infty} \kappa_\nu dz, \quad (\text{B.1})$$

We integrated along the line of sight from the site where the emission takes place, which we conservatively took as the stellar surface, to the observer (at infinity). In practice, we integrated up  $10^4 R_\star$ , at which point the effect of free-free absorption became negligible in all cases. The coefficient  $\kappa_\nu$  is (e.g. Cox 2000)

$$\kappa_\nu = 3.692 \times 10^8 \left(1 - e^{-h\nu/k_B T}\right) Z^2 g T^{-1/2} \nu^{-3} n_e n_p [\text{cm}^{-1}], \quad (\text{B.2})$$

where  $\nu$  is the frequency of the observed emission,  $h$  is the Planck constant,  $k_B$  is the Boltzmann constant,  $Z$  is the ionization state (+1 for a fully ionized hydrogen medium),  $T$  is the temperature of the medium (which in this case is  $T_c$ , since we assume an isothermal wind), and  $n_e$  and  $n_i$  are the electron and ion number density, respectively. All magnitudes are in cgs units. Since we have a fully ionized hydrogen plasma,  $n_i = n_p = n_e$ , where  $n_p$  is the proton density.

Finally,  $g$  is the Gaunt factor, which in the radio regime is given by (Cox 2000):

$$g = 10.6 + 1.9 \log_{10}(T) - 1.26 \log_{10}(Z\nu). \quad (\text{B.3})$$

## Appendix C: Other geometric configurations yielding non-detections of SPI

We show in Figs. C.1 and C.2 sketches for the alternative geometric configurations # 2 and # 3 depicted in Figure 7. Those configurations maximize the probability of non-detection of SPI (see Sect. 5.3 for details).

## Appendix D: Stokes V dynamic spectra

We show here all Stokes V dynamic spectra for all observing epochs, but the 30 October 2021, which is shown in Fig. 3. Note that all dynamic spectra are featureless, indicating that there is

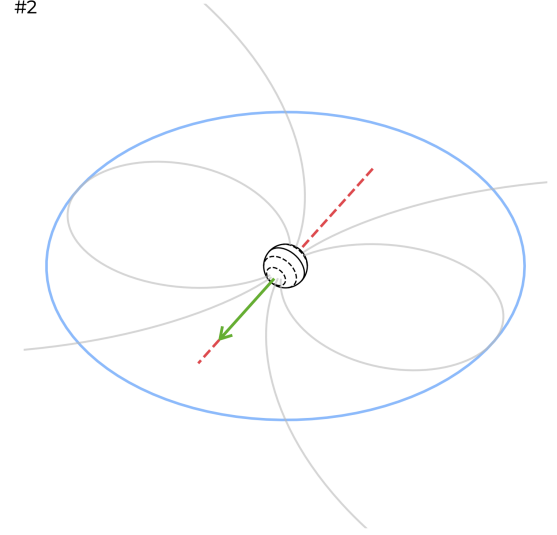


Fig. C.1: Sketch of the geometry # 2 inferred for the GJ 486 planetary system, based on our non-detection of star-planet interactions at radio wavelengths. The system is viewed pole-on, and has a low magnetic obliquity.

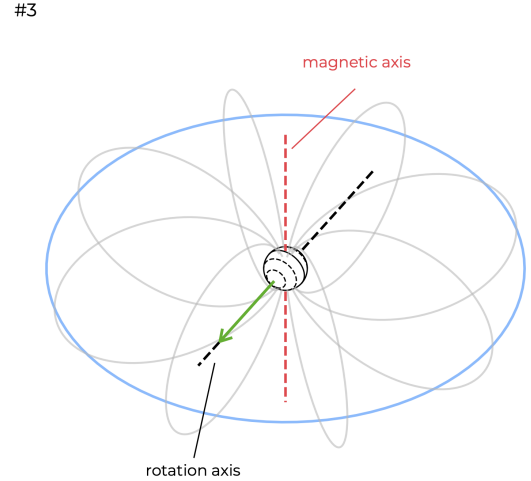
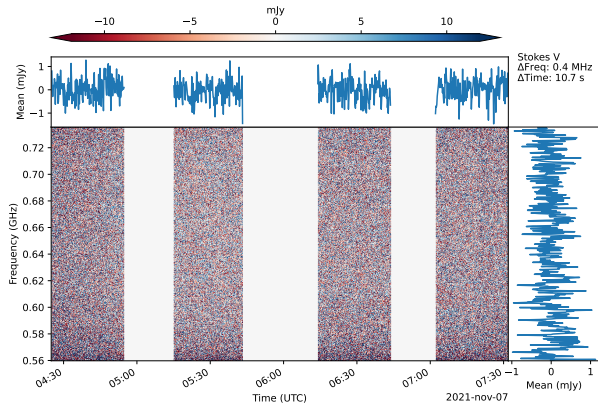


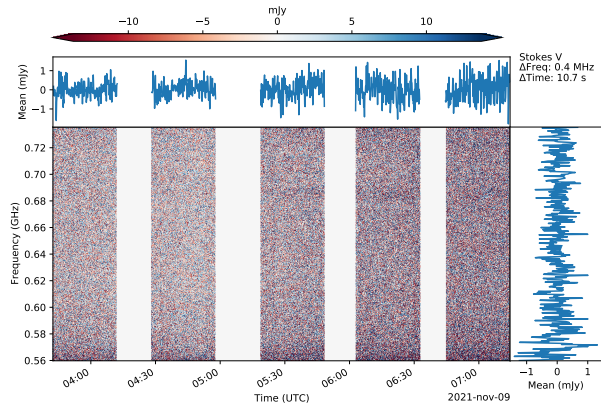
Fig. C.2: Same as in Fig. C.1, but for our system viewed pole-on and with a magnetic obliquity close to  $90^\circ$  (geometry # 3).

no bursting emission. The only possible exception is a burst-like signature around 07:00 hr on 20 November 2021. To determine whether this feature corresponded to a real emission, we obtained the dynamic spectra using four different phase centers. The resulting spectra had always the same feature seen in the original dynamic spectrum (centered at the position of GJ 486), implying that this bursting feature is not real, but due to an instrumental effect.

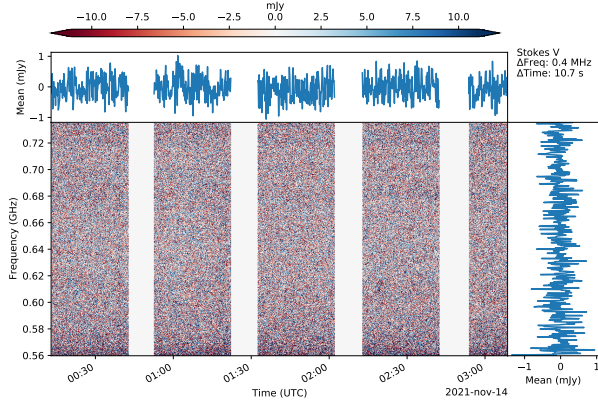




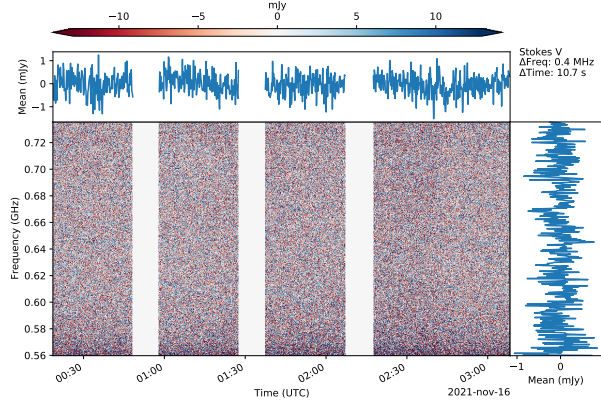
(a) Stokes V dynamic spectra for 7 November 2021.



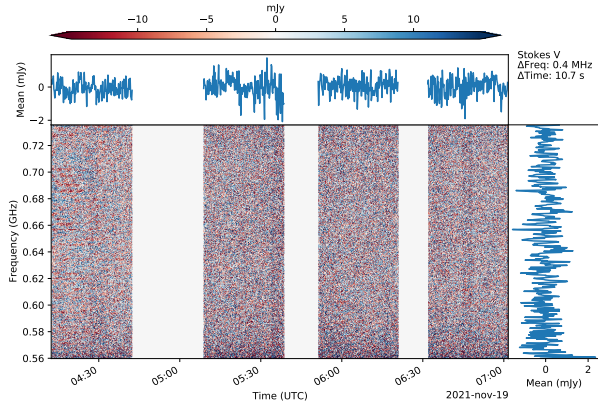
(b) Stokes V dynamic spectra for 9 November 2021.



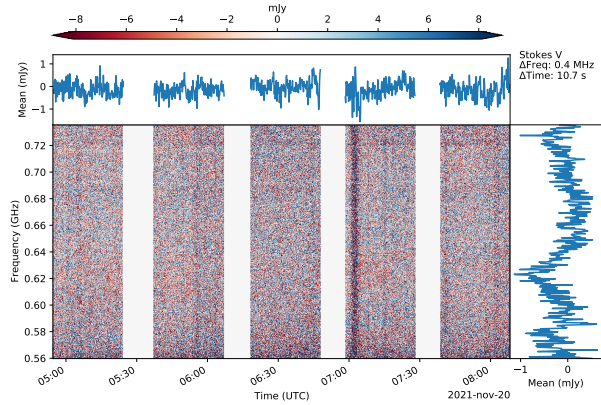
(c) Stokes V dynamic spectra for 14 November 2021.



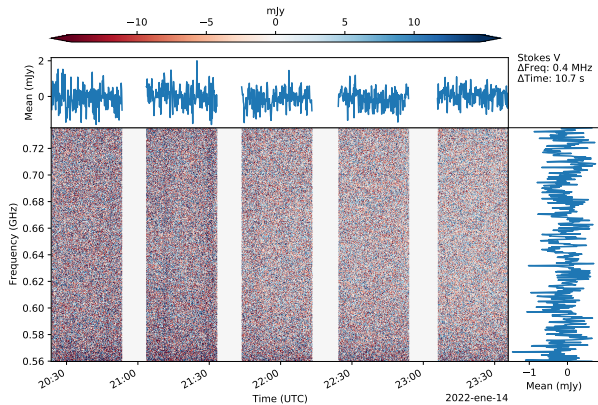
(d) Stokes V dynamic spectra for 16 November 2021.



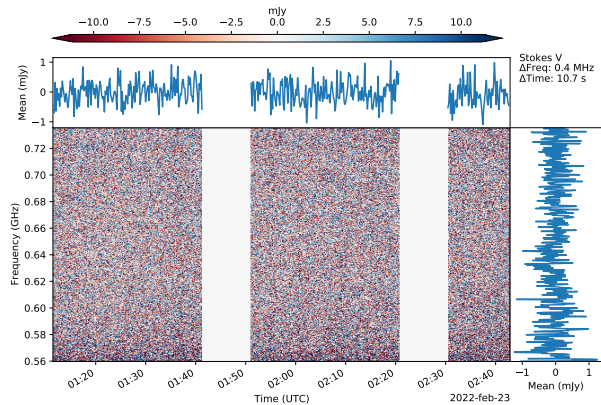
(e) Stokes V dynamic spectra for 19 November 2021.



(f) Stokes V dynamic spectra for 20 November 2021.



(g) Stokes V dynamic spectra for 14 January 2022.



(h) Stokes V dynamic spectra for 22 February 2022.

Fig. D.1: Stokes V dynamic spectra for the rest of the observing sessions. Each dynamic spectra has two other spectra associated, one collapsed in frequency and the other in time.